drones

Article

An Intelligent Fault Diagnosis Approach for Multirotor UAVs Based on Deep Neural Network of Multi-Resolution Transform Features

Luttfi A. Al-Haddad [1] and Alaa Abdulhady Jaber [2,*]

[1] Training and Workshop Center, University of Technology—Iraq, Baghdad 19006, Iraq
[2] Mechanical Engineering Department, University of Technology—Iraq, Baghdad 19006, Iraq
* Correspondence: alaa.a.jaber@uotechnology.edu.iq

Abstract: As a modern technological trend, unmanned aerial vehicles (UAVs) are extensively employed in various applications. The core purpose of condition monitoring systems, proactive fault diagnosis, is essential in ensuring UAV safety in these applications. In this research, adaptive health monitoring systems perform blade balancing fault diagnosis and classification. There seems to be a bidirectional unpredictability within each, and this paper proposes a hybrid-based transformed discrete wavelet and a multi-hidden-layer deep neural network (DNN) scheme to compensate for it. Wide-scale, high-quality, and comprehensive soft-labeled data are extracted from a selected hovering quad-copter incorporated with an accelerometer sensor via experimental work. A data-driven intelligent diagnostic strategy was investigated. Statistical characteristics of non-stationary six-leveled multi-resolution analysis in three axes are acquired. Two important feature selection methods were adopted to minimize computing time and improve classification accuracy when progressed into an artificial intelligence (AI) model for fault diagnosis. The suggested approach offers exceptional potential: the fault detection system identifies and predicts faults accurately as the resulting 91% classification accuracy exceeds current state-of-the-art fault diagnosis strategies. The proposed model demonstrated operational applicability on any multirotor UAV of choice.

Keywords: UAV; fault diagnosis; discrete wavelet transform; deep neural network

Citation: Al-Haddad, L.A.; Jaber, A.A. An Intelligent Fault Diagnosis Approach for Multirotor UAVs Based on Deep Neural Network of Multi-Resolution Transform Features. *Drones* **2023**, 7, 82. https://doi.org/10.3390/drones7020082

Academic Editors: Ziquan Yu and Youmin Zhang

Received: 28 December 2022
Revised: 20 January 2023
Accepted: 21 January 2023
Published: 24 January 2023

1. Introduction

This paper proposes an innovative method for diagnosing faults in unmanned aerial vehicles to monitor drone health parameters and detect their units' technical conditions. This technique can be incorporated into real-time control systems directly embedded in a small unmanned aerial vehicle and remote-control systems that generate a control action via satellite-tracking networks.

Generally speaking, testing fault diagnosis models on small UAVs can avoid catastrophic circumstances, save time, and ease affordability. Vibration-based fault diagnosis models and techniques for helicopters have recently emerged. The faults of the gear transmission of a specific military helicopter were diagnosed based on the vibroacoustic technique in [1]. In contrast, the vibration signals for fault diagnosis in a planetary gear train of a helicopter were employed by the authors of [2]. Therefore, and due to the similarity of the operational concept in multirotor UAVs and helicopters, improvements to the fault diagnostic model for multirotor UAVs have emerged in recent studies.

Individuals, businesses, and the government increasingly use UAVs for various objectives. Despite this being favorable, UAVs face the same physical threats as airplanes and unmanned technologies. Given the continuously expanding quantity of UAVs, these threats are becoming more plausible. There are security hazards in addition to system failures. UAVs are often operated remotely, thus, this opens the door to cyberattacks. Drones are susceptible to cyberattacks. However, real-time fault diagnosis embedded systems can compensate for this. Drone communications' security challenges, potential threats, strikes, and prevention methods, were investigated by [3]. The drones' communication protocol security analysis was also addressed in [4].

The ever-expanding spectrum of applications for unmanned aerial vehicles (UAVs), such as volcano monitoring [5], detection of rare earth elements [6], building inspecting [7], and firefighting [8], is leading to the development of more complex systems. The higher the complexity of the UAV, the more likely a component may fail. Because drones often operate close to humans, the dependability of flying robots, which directly influences the degree of safety, is becoming more critical. Reliability and high safety are essential for autonomously operated flying robots, particularly in transportation and entertainment applications. New strategies for sensor data set fusion, fault diagnosis, fault-tolerant estimation, and fault-tolerant management have obtained recent field-of-study attention. Thus, recent studies have reviewed current and previous fault diagnosis approaches in UAVs [9]. Moreover, Table 1 lists selected studies employing machine learning (ML), deep learning (DL), and signal processing approaches on UAVs.

Table 1. Selected existing studies employing machine/deep learning and signal processing methods.

Ref.	Utilized Machine/Deep Learning and Signal Processing Approach	UAV Type
[10]	Signal Analysis based on Chaos using Density of Maxima (SAC-DM) and Fast Fourier Transform (FFT)	Brushless Direct Current (BLDC) motors' behavior in a drone
[11]	Novel Deep Residual Shrinkage Network with a wide convolutional layer (1D-WIDRSN)	Quadrotor propellers with minor damage
[12]	Convolutional Neural Network	Carbon Z T-28 fixed-wing-type UAV fault simulators
[13]		Tool Wear in Aerospace Manufacturing Processes
[14]		Real aircraft fault text data set
[15]	Auto Sequential Random Forest	Quadrotor sensor fault

Most studies' main drawback in observing UAV unit conditions and constraints is that they diagnose the multirotor UAV status at a specific period without considering the influence of accumulated faults, for instance, a delay in the response time of motors, adjustments in parameters within the initial stages of a failure, or an alteration in the smoothness of the reaction to a climb, as most intelligent drones are manufactured with a clever system to avoid faults, particularly in stabilization. Additionally, there is a significant shortage of combined integrated techniques explored in publications that implement signal processing, especially multi-resolution analysis and deep neural networks. Thereby, the innovation and contributions of the monitoring and diagnostic methodology presented hereunder in this research are the following:

1. Stating the main drawbacks in recently published studies on multirotor UAVs' condition monitoring.
2. The implementation of a hybrid signal processing-based discrete wavelet transform and a deep neural network model of an original-equation-derived structure to observe UAV vibration signals.
3. Quantifying the probability of defects and pre-failure situations over a long period to create a convenient accumulated depiction of specifications considering the cumulative fault impact.
4. Presenting a versatile and risk-free experimental methodology in acquiring vibration signals of any multirotor UAV.

In terms of this paper's organization, Section 2 elaborates the different kind of UAV faults while Section 3 describes the theoretical basis of discrete wavelet transform (DWT) and DNN. The experimental setup and the adopted methodology of the suggested data calculation method, including the software block diagrams of the utilized system, are presented in Section 4. Section 5 identifies the outcomes for which a discussion utilizing figures and evidence is warranted. The conclusion is then provided in Section 6.

2. UAV and Multirotor UAV Faults' Classification

Regarding the classification of various unmanned aerial vehicles, they can be categorized based on a simple, straightforward criterion. Figure 1 depicts the division of the UAV based on the type of construction. Fixed-wing, flapping wing, tiltrotor, and rotary wing UAVs can be distinguished, while rotary wing UAVs can be subdivided into single-rotor and multirotor UAVs.

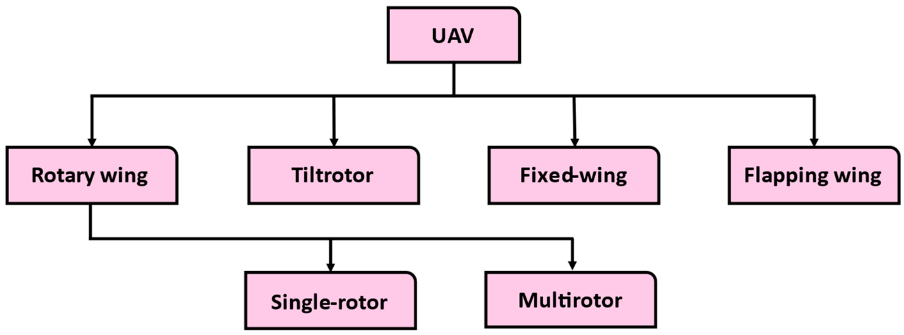

Figure 1. UAV types (based on [9]).

A selection of 152 incidents and crashes using Remotely Piloted Aircraft Systems, often known as "drones," was studied in [16]. The data were obtained during a ten-year span, from 2006 to 2015, from a limited population due to the paucity of reports. Sorting safety incidents utilizing Remotely Piloted Aircraft Systems (RPAS) into discrete categories reveals various contributing causes. The bulk of RPAS incidents included system component failures resulting from equipment issues. Airworthiness should precede pilot certification when regulating the Remotely Piloted Aircraft System business. Consequently, fault diagnostic strategies for UAVs have increased in recent years.

Generally speaking, when multirotor UAVs are diagnosed with a system component failure from equipment issues, it can be classified into two categories: sensor and actuator. The investigation in [9] supported the same categorization.

2.1. Sensor Faults

A range of guidance and payload sensors are used by aerial vehicles to enhance their operational capabilities or for data-collecting objectives in embedded systems. The delivered measures are used for control, navigation, surveillance, etc. The performance of these UAVs relies heavily on the correct and dependable functioning of the embedded sensor system. The sensors of UAVs are regularly subjected to unanticipated condition changes, which, in conjunction with the demanding flying environment, raises the danger of sensor failure, which might result in the entire loss of the aircraft. Inaccurate flight altitude estimations, for instance, may lead to a car accident with severe repercussions, including vehicle destruction, property damage, and/or human casualties. To maintain the safety of a flight, dependable functioning and successful completion of scheduled missions must be ensured by rapid identification of sensor faults.

2.2. Actuator Faults

The actuators comprise essential electrical and mechanical equipment that operate UAVs. Possible failures may lead to flying issues, resulting in vehicle crashes and potential catastrophes, and severe civilian casualties. Thus, it is evident that identifying problems in actuators is vital and that developing suitable techniques is necessary.

Flight surface actuators (rudders, ailerons, and elevators) and motors/propellers are the two primary subcategories of UAV actuators. The majority of researchers studied the faults in flight surface actuators, according to a published study [9]. Therefore, since most unregistered multirotor UAV accidents result from damaged or consumed blades, this investigation chose to diagnose faults with multirotor UAV propellers.

3. Theoretical Basis

3.1. Discrete Wavelet Transform

Signals from faulty components exhibit non-stationary behavior. However, if the frequency section of non-stationary signals is computed using the Fourier transform, the results will reflect the frequency composition averaged across the signal period [17,18]. Time–frequency analysis techniques are suitable for non-stationary transformations due to this differentiating feature. Numerous time–frequency analysis methodologies [19], such as wavelet transforms, have been used for flaw discovery and diagnosis. This technique is evaluated to establish its primary advantages and reasons for use.

The wavelet transform (WT) was developed and utilized in numerous applications to alleviate the resolution limitation of Fourier transforms [20]. Trigonometric functions are employed in the Fourier series to modify the signal to provide a collection of coefficients; in the wavelet series, the primary mother wavelet is fitted to the signal, followed by the inner product of the inspected signal and a succession of daughter wavelets. Using the scaling (s) and shifting (n) parameters, the daughter wavelets are formed by shifting and scaling the wavelet transform. The scaling of the mother wavelet is exposed to expansion or dilation; if the wavelet is enlarged horizontally, it is compressed in the vertical axis to ensure the power density of the scaled wavelet and the original primary mother wavelet are identical [21]. In the shifting stage, the wavelet is moved down the x-axis until it entirely covers the studied signal, which may be expressed as follows mathematically [22]:

$$WT(n,s) = \frac{1}{\sqrt{s}} \int_{-\infty}^{+\infty} x(t)\Psi\left(\frac{t-n}{s}\right)dt \tag{1}$$

$WT(n,s)$ is described as the wavelet transform portion of the signal $x(t)$, and $\Psi(t)$ is subsequently described as the transforming function (or the mother wavelet). The mother wavelet begins and ends, unlike the endless trigonometric functions. The mother wavelet fits the signal locally, not globally. Thus, it is the best method for accurately analyzing the projected quad-copter vibration signal.

The continuous wavelet transform (CWT) improves signal processing accuracy; nevertheless, it is potentially infinitely redundant, considering it unmanageable [23]. This increases the amount of power, computation time, and memory required, making the CWT unusable in many cases, mainly when performing wavelet analysis in real time on embedded systems or other real-time monitoring systems, as is the case here. To conserve time and energy, the DWT was developed, in which the primary mother wavelet is only scaled and adjusted at discrete moments along with the signals rather than continuously. DWT is often used to deconstruct the original signal into many signals, each with a specific frequency bandwidth and capable of being considered as a separate signal on which alternative studies may be conducted. The DWT's strength is that it evaluates data at different scales using filters with numerous cut-off frequencies. A high-pass (HP) filter is used to examine high frequencies, followed by a low-pass (LP) filter to analyze low frequencies. A complex-valued modification and augmentation to the basic DWT with essential qualities such as multi-resolution, limiting representation, and the ability to eliminate aliasing issues caused by the overlap of opposing-frequency pass-bands of the wavelet filters, the dual-tree complex wavelet transform represents another type of wavelet analysis known as complex wavelet transform [24,25]. For deconstructing and rebuilding, the dual-tree technique employs two concurrent DWTs with different low-pass and high-pass filters in each scale. The two DWTs use two pairs of filtrations, each of which passes the condition of complete reconstruction.

In general, employing the DWT to subdivide time-domain signals allows for multi-resolution analysis in many frequency bands with varying resolutions [26]. The DWT utilizes the wavelet and scaling function related to the HP and LP filters. The original signal $x[n]$ is separated at the first level by passing it throughout both of these filters, acquiring two resulting signals under the same sampling length as the foremost primary signal, which is referred to as coefficients. To keep the number of these factors in the filtered signals equal to the number of coefficients in the primary signal samples, the samples are down-sampled by a factor of two, with only one out of every two subsequent samples retained. Thus, the first level detail coefficients $(cD1)$ are the returned signal coefficients from the HP filter after down-sampling. These coefficients include the high-frequency info of the primary signal, while the coefficients recovered from the LP filter and again after the down-sampling procedure are known as the first level approximation coefficients $(cA1)$. These coefficients conceal the signal's low-frequency information. This is mathematically stated as [27]:

$$cD1[k] = \sum\nolimits_n x[n] * h * [2k - n] \tag{2}$$

$$cA1[k] = \sum\nolimits_n x[n] * g * [2k - n] \tag{3}$$

$h[n]$ and $g[n]$ segments denote the high-pass and low-pass filters, respectively. When the first level decomposition is achieved, the preceding technique may be reused to subdivide cA1 into additional approximation and detail coefficients, as expressed in Equations (4) and (5) [27]. This technique is repeated until the desired level is reached, where the decomposition must be recognized.

$$cD_l[k] = \sum\nolimits_n cD_{l-1}[n] * h * [2k - n] \tag{4}$$

$$cA_l[k] = \sum\nolimits_n cA_{l-1}[n] * g * [2k - n] \tag{5}$$

$cD_l[k]$ and $cA_l[k]$ resemble the DWT coefficients at level (l), while $cA_{l-1}[n]$ is the approximation coefficient at $(l-1)$ level. In each subdivision level, the pertaining approximation and detail coefficients have particular frequency bands defined by $\left[\frac{F_s}{2^{l+1}} - \frac{F_s}{2^l}\right]$ for the detailed coefficient cD_l and $\left[0 - \frac{F_s}{2^{l+1}}\right]$ for the approximation one; F_S stands for sampling frequency [28]. Nevertheless, filtering and subsampling at each level will deliver half the sample number (half the temporal resolution) and half the frequency spectrum (twice the frequency resolution). Due to the repeated down-sampling by two, the total number of samples in the processed signal must also be a power of two. Concatenating all coefficients starting with the last level of decomposition yields the DWT of the original signal, which has the same number of samples as the original signal. Figure 2 is a graphic representation of how multi-level subdivision is accomplished. The number of necessary decomposition levels is determined by the lowest frequency bandwidth to be monitored. In addition, the highest level of deconstruction may be achieved when the unique complexities consist of a single occurrence [28].

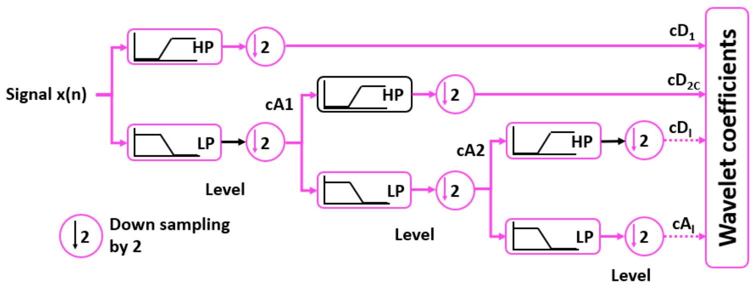

Figure 2. Signal decomposition of multi-levels employing DWT.

After calculating the detail and approximation coefficients, it is possible to reconstruct the detail and approximation waves at each level to view the data and accurately depict healthy and faulty circumstances. Each signal will have the same number of samples as the primary input signal but will have a separate frequency range. This can be achieved by up-sampling the detail (or approximation) coefficients by two, as they were initially produced by down-sampling by two, and then synthesizing them using low-pass and high-pass filters. To reconstruct the first level A1 approximation wave signal, for instance, just the approximation coefficients are required at this level, while a vector of zeros is given in place of the detail coefficients. Similarly, the same method can generate the first level detail signal D1. Figure 3 illustrates the concept of signal synthesis.

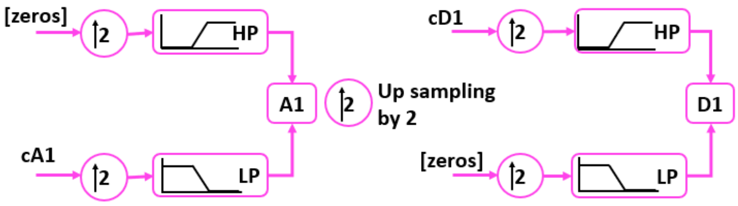

Figure 3. Reconstruction of the approximation and detail signals with zero padding.

3.2. Selection of the Optimum Mother Wavelet

DWT supports several wavelet families. To determine the best wavelet function for this study, a survey was conducted to identify the many main mother wavelets authors have used for fault diagnosis. Previous wavelet families include Daubechies (dbN), Symlets (symN), and Coiflet (coifN), where N is the number of orders in the wavelet family [29]. For example, the wavelets symN and dbN have 2N coefficients. No generalized theoretical approach has been reported for choosing the best wavelet family when researchers use multiple families to analyze the same wave signal [30,31]. In many cases, the selection is performed by trial and error [32]. Indeed, if the mother wavelet and the operative instance signal have a substantial similarity, the wavelet function is deemed suitable for evaluating the signal under consideration [33].

Certain wavelet functions, such as sym7 or db10, have multiple filter coefficients due to the increased computational load on the PC and programs, which increases the processing time required for real-time wavelet analysis. Moreover, because the remaining options are decreased and limited to lower-order families, no more quantitative procedures are necessary to pick the mother wavelet. Symelet and Daubechies families are well-known for their performance in vibration signal analysis and encompass a wide range of wavelet orders [34]; hence, Daubechies' fourth order (db4) was used in this study. Figure 4 illustrates the analysis of the discrete wavelet transform's high-pass and low-pass filters and the synthesis of the same high-pass and low-pass filters where a wavelet family of db4 is selected.

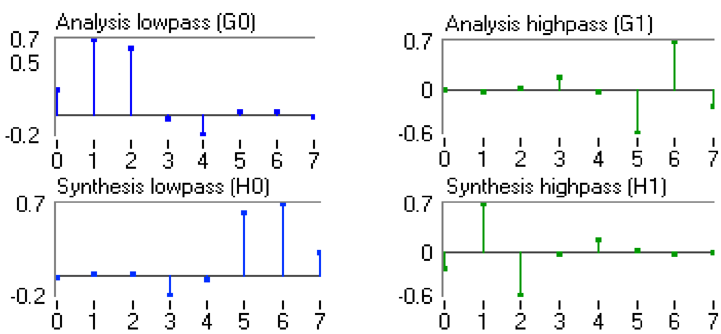

Figure 4. Daubechies order 4 (db4) mother wavelet filter coefficients.

3.3. Deep Neural Network

A deep neural network, or deep net for short, is a neural network with some amount of complexity, generally, at least two layers. Deep nets use advanced math modeling to analyze data in complicated ways. For instance, parameters θ are used to represent a neural network. Weight matrices Wi and bias vectors bi $(i = 1,\ 2,\ \ldots,\ M)$ are among the parameters, where M denotes the depth of the neural network structure or the number of hidden layers as depicted in Figure 5a. By minimizing the loss function $L_\theta\ (X)$, DNNs provide the best approximation of the original function. The neural networks under investigation in this research are multilayer feed-forward neural networks, which are composed of the alternating affine linear equation $Z = X * W + b$ where X represents the set of training data and the nonlinear function $\sigma(.)$, which are known as activation functions. The weight matrix and bias matrix alter the training data set at each hidden layer, and the result is passed back to the next hidden layer through the activation function. The neural network learning approach is based on merging numerous linear and nonlinear functions to approximate the goal Equation 6 below [35]:

$$Y = f[Net] = (\sigma_L(\sigma_{L-1}(\cdots\sigma_1(\mathrm{X}\cdot\mathrm{W}_1 + \mathrm{b}_1)\cdots)\mathrm{W}_{L-1} + \mathrm{b}_{L-1})\cdot\mathrm{W}_L + \mathrm{b}_L)\cdot\mathrm{W}_{out} + \mathrm{b}_{out} = \sigma_L\cdots\sigma_1(\mathrm{X})\cdot\mathrm{W}_{out} + \mathrm{b}_{out} \quad (6)$$

where Wi and bi $(i = 1,\ 2, \ldots,\ L-1)$ are the ith hidden layer's weight matrices and bias vectors, respectively, W_{out} and b_{out} are the output layer's parameters, and $\sigma_i(.)$ is the ith layer activation function, which is an element-wise nonlinear function. The most frequently utilized activation functions are sigmoid, tanh, and ReLU. Because the tanh function (Equation 7) is in the range $[-1, 1]$, it has the benefit of being more readily able to handle negative integers. As a result, it has been used in this investigation.

$$\tan\mathrm{h}(\mathrm{x}) = \frac{\sin\mathrm{h}(\mathrm{x})}{\cos\mathrm{h}(\mathrm{x})} = \frac{\mathrm{e}^x - \mathrm{e}^{-x}}{\mathrm{e}^x + \mathrm{e}^{-x}} \quad (7)$$

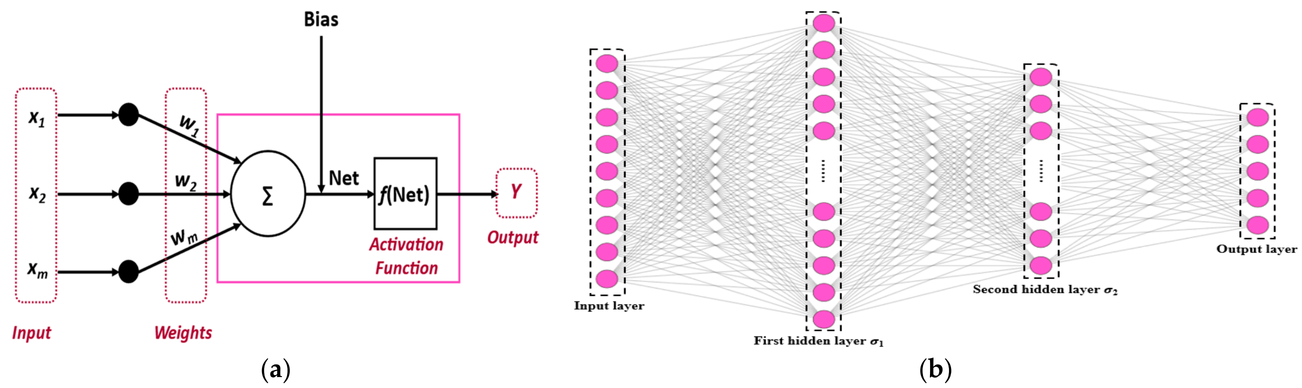

Figure 5. Neural network: (**a**) parameters; (**b**) two hidden layer illustration.

Typically, network training consists of adjusting the parameter θ based on gradient optimization during neural network backpropagation. The objective is to identify the best parameter $\theta_{optimum}$ that minimizes the loss function. This technique needs $f[Net]$ to differentiate its unknown parameters Wi and bi, namely, to further assess the proposed algorithm's differential operators. The flux gradient is significant in this procedure. It denotes the direction in which the parameters θ might change.

We understand that increasing the number of hidden layers in a single hidden layer network may result in a deep neural network. To exemplify the phrase, consider a network with two hidden layers, as illustrated in Figure 5b. The network output $f[Net]$ for the training data set $X = \{\ X_i = (u_i,\ t_i)\}_{i=1}^{N}$ may be represented as follows:

$$Y = f[Net] = (\sigma_2(\sigma_1(X_i\cdot\mathrm{W}_1 + \ \mathrm{b}_1)\mathrm{W}_2 + \mathrm{b}_2)\cdot\mathrm{W}_{out} + \mathrm{b}_{out} = \sigma_2\sigma_1(X_i)\cdot\mathrm{W}_{out} + \mathrm{b}_{out} \quad (8)$$

In this case, an assumption is that the hidden layers have N_1 and N_2 neurons. W_1, W_2, and W_{out} are thus the weight matrices of the following type:

$$W_1 = \begin{bmatrix} w_{11}^{(1)} & w_{1N_1}^{(1)} \\ w_{21}^{(1)} & w_{2N_1}^{(1)} \end{bmatrix}_{2*N_1}, W_2 = \begin{bmatrix} w_{11}^{(2)} & w_{1N_2}^{(2)} \\ w_{N_1 1}^{(2)} & w_{N_1 N_2}^{(2)} \end{bmatrix}_{N_1*N_2}, W_{out} = \begin{bmatrix} w_{11}^{(out)} \\ w_{N_2 1}^{(out)} \end{bmatrix}_{N_2*1}$$

where the weight is represented by $w_{ij}^{(k)}(k = 1, 2)$ of the ith neuron on the kth hidden layer to the jth neuron on the (k+1)th hidden layer. Consequently, b_1, b_2, and b_{out} are the bias vectors:

$$b_1 = \begin{bmatrix} \beta_1^{(1)} & \beta_{N_1}^{(1)} \end{bmatrix}_{1*N_1}, b_2 = \begin{bmatrix} \beta_2^{(2)} & \beta_{N_2}^{(2)} \end{bmatrix}_{1*N_2}, b_{out} = \begin{bmatrix} \beta^{(out)} \end{bmatrix}_{1*1}$$

The previous equations obtain the values of each quantity in Figure 6 for the previously indicated activation function:

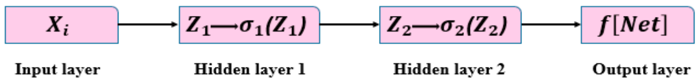

Figure 6. A neural network with two hidden layers' data transmission system.

Employing the equations mentioned above when calculating the objective gradient function with respect to the parameters, the loss at each hidden layer is computed beginning with the network output layer and progressing layer by layer until it reaches the input layer. An intelligent data mining tool sets the parameters randomly for the most optimized outcome.

4. The Experimental Approach

4.1. Drone Selection

Rapid technological improvements, particularly in the last decade, have made off-the-shelf UAVs weighing less than 250 g affordable for recreational usage by the general public. Many well-known manufacturers (for example, DJI) are now focused on this area of UAVs, and the new DJI Mini 2 [36] drone is one of many that come under this category, allowing simple access to be bought and operated with no Part 107 certification or Transmitter ID registration. Additionally, in [37], the DJI mini 2 demonstrated good applicability; therefore, the DJI mini 2 combo has been adapted in this study.

4.2. Accelerometer Selection

Even after the drone inspection method has been finished, certain hazardous circumstances are challenging to see or uncover with the unaided eye; hence, the study in [38] suggests a real-time early drone inspection approach based on vibration data. First, the detection reliability of many microelectromechanical system (MEMS) sensors was investigated and compared, including the ADXL335 accelerometer, ADXL345 accelerometer, ADXL377 accelerometer, and SW420 vibration sensor. In contrast to other MEMS sensors, the testing results demonstrated that the vibration parameter measured using the ADXL335 and ADXL345 accelerometers is the best choice since most malfunctioning conditions can be identified. The outcome of the anomaly inspection algorithm is subsequently converted into a "Healthy" or "Faulty" status, shown in a mobile application for easy monitoring. The ADXL335 is a low-power sensor with an integrated signal conditioning circuit capable of detecting static and dynamic acceleration in the 3 g range. It is considered and employed in this investigation because it is readily available in the local market; its specifications are listed in Table 2. The functioning mechanism consists of a sensor output with an amplitude proportional to acceleration.

Table 2. Specifications of the ADXL335 accelerometer.

No.	Specification	Information
1	Dimension	21 × 16 × 10 mm
2	Weight	2 g
3	Operating voltage	5 V
4	Operating current	400 µA
5	Sensitivity	300 mV/g
6	Bandwidth	0.5–1600 Hz (x- and y-axes) and 0.5–550 Hz (z-axes)
7	Full-scale range	+/− 3 g

4.3. Methodology

The experimental study is depicted in Figure 7, where the DJI Fly application is downloaded on a Note 10+ smartphone to control the hovering speed of the adopted DJI Mini 2 combo drone. ADXL335 accelerometer is fixed upon the intersection of the four blades in an X shape to gather vibration data sets using an integrated connection of a vibration accelerometer with a DAQ-6009 data collection device with a maximum analog input sampling rate of 48 kS/and 14 bits differential, 13 bits single-ended input resolution. The DAQ-6009 has eight analog inputs, three of which are used owing to the accelerometer's three axes of x, y, and z. The data capture device is then linked to a Lenovo laptop equipped with a core i7 CPU, where LabVIEW [39] is run for data gathering. The signal is then processed in DWT, where statistical features of six levels are computed and examined using feature selection methods before being routed via a deep neural network for fault detection. The global axis for the computations is represented in Figure 8, with the ADXL335 accelerometer positioned between the four blades and motors. The quadrotor's movement options include rolling along the x-axis, pitching along the y-axis, and yawing along the z-axis.

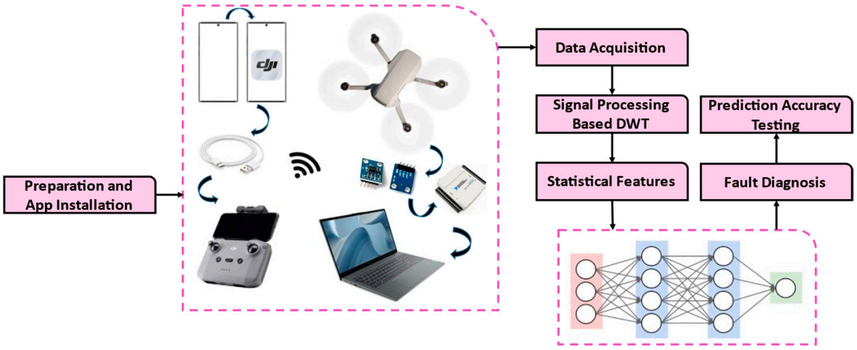

Figure 7. Experimental approach.

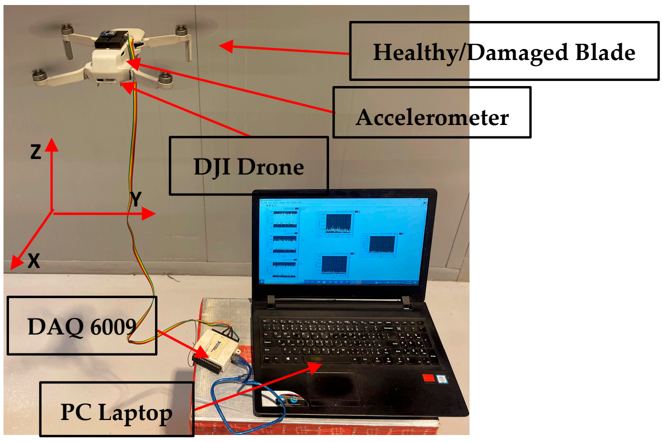

Figure 8. Location of the accelerometer on the drone and Field of Operating.

In this study, Figure 9a depicts the locations of the damaged blades. Data collection was conducted under five distinct conditions: healthy, Bottom Right (BR) blade 1 damaged, Top Right (TR) blade 2 damaged, Top Left (TL) blade 3 damaged, and Bottom Left (BL) blade 4 damaged. It is worth mentioning that the propeller construction of the DJI Mini 2 Combo brushless motor consists of two blades, one of which is damaged in this study. Concerning the location of the damaged blades (see Figure 9b), it is essential to point out that the structure and frame of the DJI mini 2 combo drone have a construction in which the bottom two blades are adjusted lower than the top two blades; these structural shapes will show the differences in the simulated faults in the discussion section of this article. By picking these four places, we assure that all stable regions will be affected by blade-damage-induced imbalances. The studied cases are listed in Table 3.

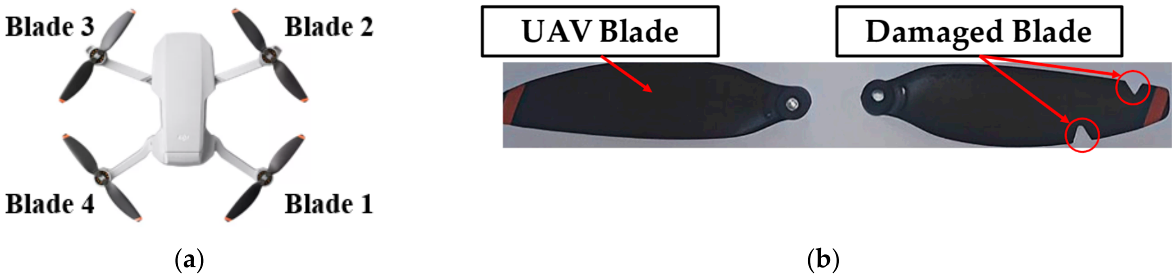

Figure 9. Fault introduction: (**a**) location of the damaged blades; (**b**) damaged blades.

Table 3. Studied cases.

Case	Hovering Speed (RPM)	Hovering Speed (Hz)	Height From Ground (m)	Location of Damaged Blade
Healthy Blade 1 Damaged Blade 2 Damaged Blade 3 Damaged Blade 4 Damaged	10,000	168	1.2	- Bottom Right Top Right Top Left Bottom Left

4.4. The Developed LabVIEW Program for Signal Processing

Figures 10 and 11 illustrate how NI LabVIEW 2020 performed a DAQ assistance function. The voltage analog input signals were collected and instantly divided by the sensitivity of the vibration sensor to convert them to g units. The signal was then separated into three output signals X, Y, and Z. Arithmetic mean (AM) was used for calibration. AM is the sum of all integers in a group divided by the number of items in the list. This is seen in Equation (9) below. A constant control subtraction of the AM is performed to calibrate the accelerometer's location continuously. The dynamic data are then examined at six levels utilizing multi-resolution analysis with DWT, as illustrated in Table 4 below. The values of each level are measured using DWT and statistical feature acquisition. For each vibration signal, all graphs are included in the measurement files.

$$AM = \frac{1}{N}\sum_{i=1}^{N} X_i \tag{9}$$

Table 4. DWT Level's frequency.

Levels	1	2	3	4	5	6	Approx
Frequency Range (Hz)	1024–512	512–256	256–128	128–64	64–32	32–16	16–0

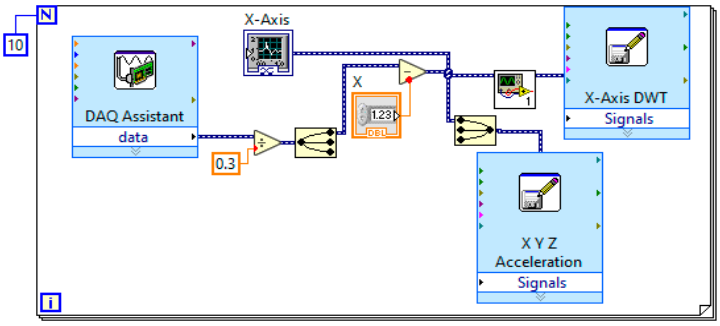

Figure 10. Sample code from the overall time-domain adopted block diagram.

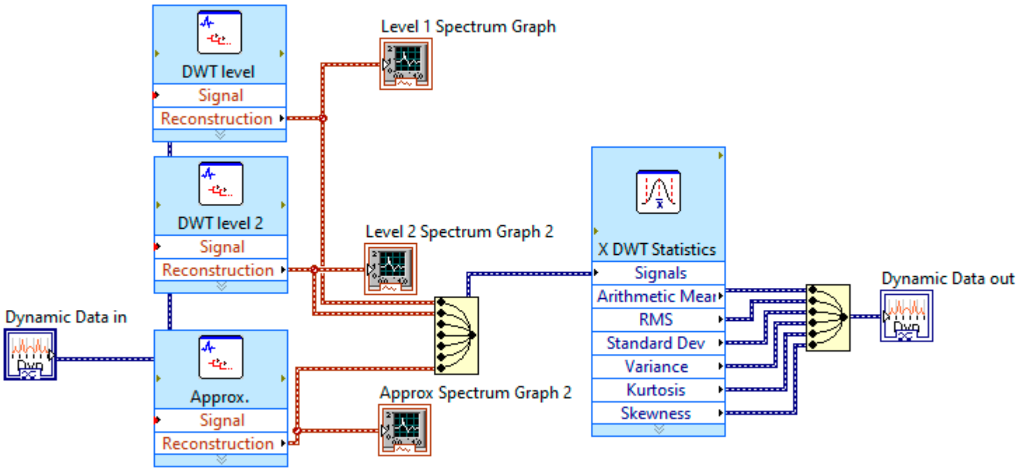

Figure 11. Sample code from the overall time–frequency domain adopted block diagram.

4.5. Signal Analysis

Because of their effectiveness in forecasting problems, vibration signals have been widely used in recent studies [40–46]. Using the NI LabView 2020 signal processing software, the accelerometer voltage measurements were gathered and translated into time-domain acceleration signals. Because the motors operate at around 168 Hz, a frequency range of 1024 Hz was used. A sampling rate of 512 samples per second was used. Figure 12a–c show the time-domain vibration data for the different health states for the x, y, and z axes, respectively. The statistics also show the amount of data collected in one second, 1024 vibration signals. Additionally, time-domain vibration signals of the damaged blade 1 are depicted in Figure 12d–f.

Figure 13a,b display the time-domain wavelet decomposition in six wavelet levels and a detailed wavelet of two studied cases, the healthy state and blade 1 damaged state, respectively. Level 1 has a frequency range of [1024 to 512] Hz, followed by level 2 with a frequency range of [512 to 256] Hz. Level 3 has a frequency range of 256 to 128 Hz. Level 4 decomposition happens in a frequency range of [128 to 64] Hz. Levels 5 and 6 have frequency ranges of [64 to 32] Hz and [32 to 16] Hz, respectively. Finally, the approximation level has a frequency range of [16 to 0]. As previously stated in the examined cases, the drone will hover at a constant speed of 10,000 RPM with a frequency of roughly 168 Hz.

Interestingly, the largest disturbed amplitudes were observed at levels 2 and 3 as blade 1 damaged state has larger amplitudes than the healthy state, indicating fault existence. Because the hovering frequency is 168 Hz, it was expected that level 3 would seem to be more suited for obtaining statistical information. Nonetheless, level 2 displays similarly disturbed amplitudes because the DJI mini-2's brushless motors try to rebalance themselves correspondingly. When confronted with an imbalance, the actuators will spin faster or slower than the input hovering speed, depending on the fault induced by the blade. Nonetheless, upcoming important feature selection procedures indicate whether levels 1, 2, and 3 are the most relevant levels for acquiring statistical features and if the disturbances removed from deeper levels are valuable indications of a fault in the UAV blade.

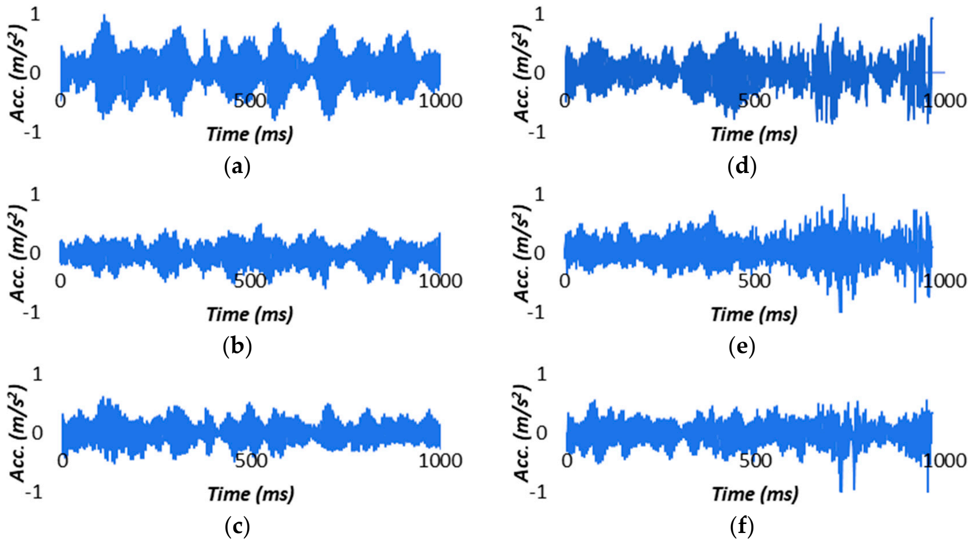

Figure 12. Vibration signals of (**a**) healthy state x-axis; (**b**) healthy state y-axis; (**c**) healthy state x-axis; (**d**) blade 1 damaged state x-axis; (**e**) blade 1 damaged state y-axis; (**f**) blade 1 damaged state z-axis.

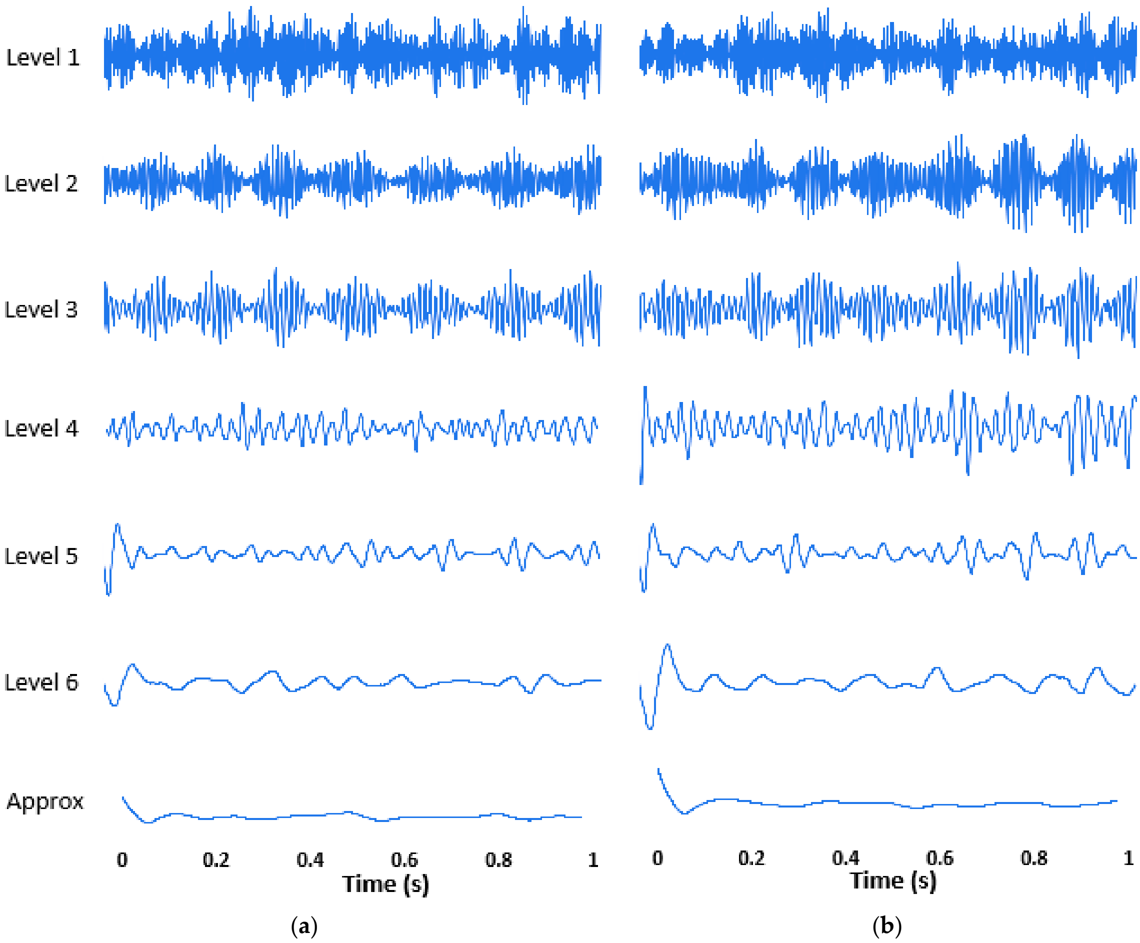

Figure 13. Time–frequency pitching vibration signal decomposition of levels 1–6 and the approximation level, respectively, of the studied case when: (**a**) healthy, (**b**) blade 1 is damaged.

4.6. Statistical Features and Important Feature Selection

Time–frequency domain analysis is commonly used to monitor the status of several applications, including quad-copters. Root mean square (*RMS*), variance (*V*), standard deviation (*SD*), kurtosis value (*KV*), and skewness (*S*) are among the statistical characteristics employed in this work's time–frequency domain study to determine quad-copter health condition. The statistical features significantly impacted pattern recognition ability and were chosen due to their efficacy in prior investigations [47]. The following equations of statistical features were derived and employed to detect initial quad-copter damage:

$$RMS = \sqrt{\frac{1}{N}\sum_{i=1}^{N}(X_i)^2} \tag{10}$$

$$V = \frac{1}{N}\sum_{i=1}^{N}(X_i - AM)^2 \tag{11}$$

$$SD = \sqrt{\frac{1}{N}\sum_{i=1}^{N}(X_i - AM)^2} \tag{12}$$

$$KV = \frac{\frac{1}{N}\sum_{i=1}^{N}(X_i - AM)^4}{RMS} \tag{13}$$

$$S = \frac{1}{N-1}\sum_{i=1}^{N}(X_i - AM)^3 \tag{14}$$

This means that there are five features for each level of decomposition; hence, 35 features for each axis were utilized in the calculations. When there are too many features, overfitting arises. Choosing the right features for training and testing data is critical for improving model performance. Noting that features 1–5 are the five features of the first level, 6–10 are the five features of the second level, 11–15 are the features of the third level, 16–20 are the features of the fourth level, 21–25 are the features of the fifth level, 26–30 are the features of the sixth level, and, finally, 31–35 are the features of the approximation level, respectively. It is paramount to point out that x and z axis features were excluded from computations due to their minor efforts as the vibration pitches more than it rolls or yaws.

4.6.1. ReliefF

Relief algorithms are efficient and general-purpose attribute estimators. They may find attribute conditional connections in regression and classification and provide a unified picture of attribute estimates. Furthermore, their evaluations of quality have a natural meaning. While they are often thought of as feature subset selection procedures used before learning a model, they have been effectively applied in various scenarios. ReliefF and Gain Ratio have shown remarkable potential in detecting important features [48]. The closest same-class instance is called a "near-hit," whereas the closest different-class instance is called a "near-miss." The weight vector is updated using Equation (15) below.

$$Wi = Wi - |Xi - nearHitx| + |Xi - nearMissx| \tag{15}$$

Thus, the weight of any given feature decreases as it varies from that feature in adjacent examples of the same class more than it differs from that feature in neighboring examples of the other class and rises when the converse is true. After a few repeats, divide each item of the weight vector by the number of iterations. This is the most important vector. If the relevance of a feature surpasses a certain level, it is picked

4.6.2. χ^2

The χ^2 statistical optimal feature selection approach was employed to improve prediction accuracy [49]. The performance of the proposed model was then verified by comparing it to standard models using numerous performance criteria. The suggested model improved precision from 85.29% to 89.7%. Furthermore, the componential load was cut in half. Therefore, it was also implemented in this study. Figure 14 depicts the results of both functions. Nine features were selected depending on the figures: SD Level 1, V Level 1, RMS Level 1, RMS Approximation Level, V Level 2, S Level 2, S Level 1, SD Level 2, and RMS Level 2. The results are compatible with the findings in Section 4.5.

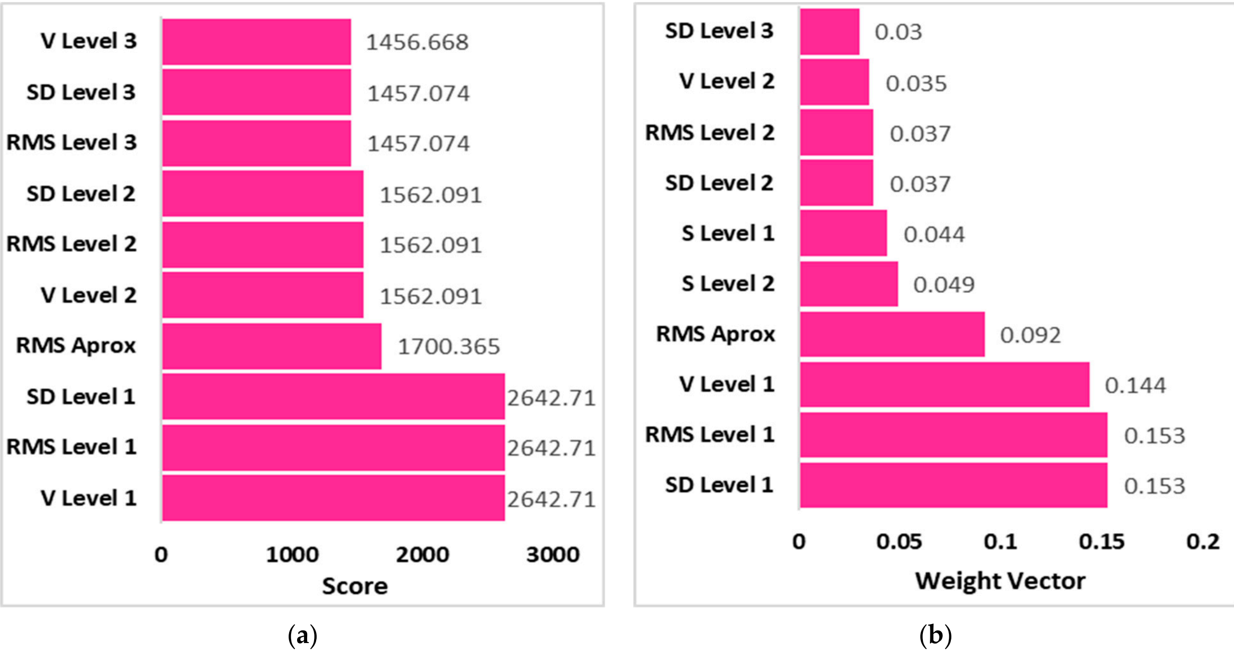

Figure 14. Top 10 statistical features' ranking: (**a**) χ^2; (**b**) ReliefF.

4.7. The Developed Orange Program for Deep Neural Network

After loading the CSV excel file into the widget of Orange data mining [50], as depicted in Figure 15, the columns were picked to determine all 35 attributes in a ranking manner based on Section 4.6. Nine characteristics were picked, resulting in nine input neurons. As stated in Section 3.3, the deep neural network comprises two hidden layers. The first hidden layer contains 40 neurons, whereas the second contains 20 neurons, and, finally, the last output layer contains 5 neurons related to the five studied cases. Although it is known that fewer neurons and more layers improve classification accuracy, two hidden layers were sufficient for the classification strategy. Using a data sampler, 66.66% of the input data were for training, and the remaining 33.33% were employed for the designed DNN testing, with the confusion matrix of the resulting model displayed. A total of 8000 readings were taken, with each state receiving 1600 statistical readings. In addition, a prediction criterion was employed to forecast fresh unused readings when the distributions were displayed. Adam solver was utilized in the deep neural network with a maximum number of iterations of 200 in a replicable training condition. Nonetheless, and due to the flexibility of Orange data mining, this orange assembly and deep neural network are of flexible applicability, starting with the vibration signals acquired from a shaft of a brushless motor [51] and ending with the sensor depth readings of utilizing plastic waste bottles on soil response above buried pipes [52], among other wide applications.

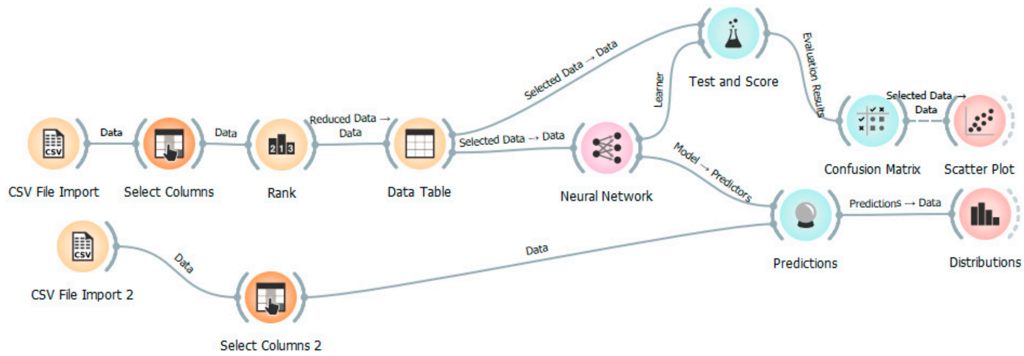

Figure 15. Orange widgets' diagram.

5. Results and Discussion

5.1. Test and Score

Tables 5 and 6 describe the performance of the DNN models. Table 5 shows the results of the DNN model before the significant feature selection strategy, whereas Table 6 shows the results of the same DNN model after the important feature selection approach. Both models' training and testing times were identical, with 25 seconds spent training 66.66% of the data and 0.06 seconds spent testing the remaining 33.33%. Interestingly, when all 35 characteristics were incorporated, the classification accuracy of the basic model was 54.1%, but the enhanced model with nine features input displayed excellent classification accuracy with an enhanced percentage of 91%. Following the use of essential feature selection procedures, there was an improvement in accuracy, with a total percentage value of 36.9%. Furthermore, when classification accuracy increased, precision and recall increased proportionally. However, several assessment factors were not significantly influenced. The specificity was enhanced from 88.5% to 97.8%, and the area under the curve, AUC, was also improved from 83.1% to 98.7%.

Table 5. Model results' evaluation before feature ranking.

Evaluation Results	Train time (s)	Test time (s)	Area under Curve (AUC)	Classification Accuracy (CA)	Precision	Recall	Specificity
Value	25.602	0.064	0.831	0.541	0.54	0.541	0.885

Table 6. Model results' evaluation after feature ranking.

Evaluation Results	Train time (s)	Test time (s)	Area under Curve (AUC)	Classification Accuracy (CA)	Precision	Recall	Specificity
Value	25.093	0.057	0.987	0.91	0.91	0.91	0.978

Regarding the explanation of the findings, the confusion matrices for both models were highlighted. Figure 16a illustrates the confusion matrix of the DNN model prior to the application of important feature selection strategies. Presented is the actual value of each of the five examples, where the total number of occurrences was 8000 divided by 5, yielding 1600 samples per case. As signals from blade 4 and blade 3 (left side of the drone) are partly misinterpreted as healthy states, the predicted values for the healthy condition are 2063 instances. More than half of the data were scattered between healthy and damaged blade 3 states, making it impossible to anticipate the condition where blade 4 was damaged. In contrast, the right side of the drone performed marginally better since the damaged statuses of blades 1 and 2 were partly anticipated accurately. With this model, fault diagnosis may only be performed to determine if a defect is present; the location of the damaged blade cannot be identified.

Predicted

Actual	Blade 1	Blade 2	Blade 3	Blade 4	Healthy
Blade 1	936	243	120	119	182
Blade 2	211	1189	64	42	94
Blade 3	69	82	821	300	328
Blade 4	91	77	506	426	500
Healthy	76	74	252	239	959
Σ	1383	1665	1763	1126	2063

(**a**)

Predicted

Actual	Blade 1	Blade 2	Blade 3	Blade 4	Healthy
Blade 1	1598	0	2	0	0
Blade 2	0	1528	34	5	33
Blade 3	3	7	1579	0	11
Blade 4	0	1	0	1324	275
Healthy	0	29	14	304	1253
Σ	1601	1565	1629	1633	1572

(**b**)

Figure 16. Confusion matrices: (**a**) before important feature selection, (**b**) after important feature selection.

After implementing two important feature selection methods to the DNN model, an improved model with high classification precision is achieved. Figure 16b exhibits the confusion matrix of the enhanced DNN model. Blade 1's damaged state, blade 2's damaged state, and blade 3's damaged condition were successfully anticipated. The right side and upper left corner of the drone have a high fault classification. However, interference occurs between the damaged condition of the fourth blade and the healthy state of the drone. A total of 304 occurrences out of 1600 healthy-state instances are misdiagnosed as blade-4-damaged, while 275 instances out of 1600 blade-4-damaged-state cases are misdiagnosed as healthy. This is explained in Figure 16. The x-axis indicates the variance of level 1 decomposition, and the y-axis represents the RMS of the same level. Figure 17 illustrates the scatter plot acquired from the enhanced model's confusion matrix where the five examined states are presented, with the x-axis representing the variance and the y-axis representing the RMS. These axes were randomly chosen to present the data in how they were ranked using significant feature selection approaches. The aggregation of all five states is appropriately presented. The first blue cluster represents the state in which blade 1 is damaged, the second red cluster represents the condition in which blade 2 is damaged, and the third green cluster describes the situation in which blade 3 is damaged. Lastly, the brown and yellow clusters indicate the damaged state of blade 4 and the healthy state of the drone, respectively. There is such a noticeable interference between the obtained data of these states that the clusters seem almost similar. This may be explained by the fact that the damaged blade has such little effect on the drone that it can still be considered a healthy, functioning drone.

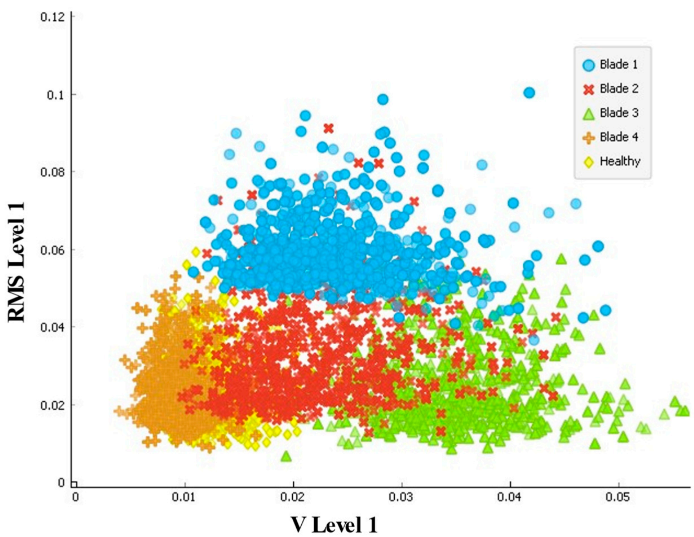

Figure 17. Five studied cases' clustering.

5.2. Model Validation

To further corroborate the classification results, additional data sets were used to develop a prediction criterion based on one hundred distinct statistical features for four studied cases where blades numbered 1 through 4 were damaged. Figure 18 depicts the performance of the predictive model.

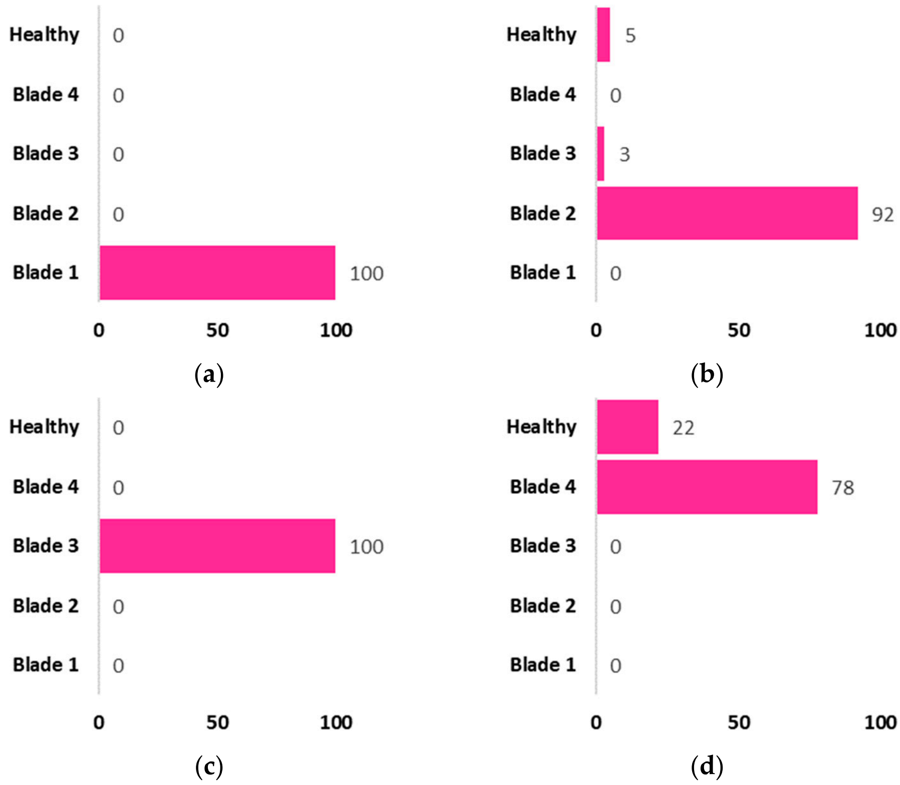

Figure 18. Prediction results: (**a**) Damaged blade 1. (**b**) Damaged blade 2. (**c**) Damaged blade 3. (**d**) Damaged blade 4.

As displayed in Figure 18a, the statistical features of the data set when blade 1 was damaged, located in the lower half of the drone, were accurately predicted with a classification accuracy of 100 percent. Intriguingly, a classification accuracy of 92% was achieved when blade 2 was damaged. These results contradict the frame construction of the DJI mini 2 combo since the drone's top half is more stable than its lower half. Nonetheless, this may be adequately explained by the fact that these vibrations are all related to the frame, regardless of where the damaged drone is located. In addition, the prediction model was applied to the data set in which blade 3 is harmed, where a 100 percent accurate prediction was observed in Figure 18c. Lastly, the categorization results for the damaged blade no. 4 are similarly inconsistent. Seventy-eight instances were accurately predicted, whereas the remaining 22 were predicted as if the drone was operating in a healthy state. This is consistent with the results of the trained–tested model presented in the confusion matrices. Compared to other state-of-the-art fault diagnostic methods, the overall forecast accuracy of this model is excellent.

6. Conclusions

This study presented the results of establishing a combined method to diagnose the operating state of a multirotor UAV. Prior to a multi-resolution wavelet decomposition analysis, a deep neural network architecture was designed to implement improved statistical features, permitting the monitoring of the deviation of parameters from the predicted values and detecting defects and pre-failure states.

A six-level decomposition of the time-domain wavelet using discrete wavelet transform into a time–frequency domain was performed to obtain statistical features. As a result, the parameters obtained from this study's theory are significantly more robust than those obtained from the total time-domain signal. Furthermore, the combination of important feature selection approaches and deep neural networks has shown considerable potential in identifying defects in hovering multirotor UAVs. Although induced non-stationary vibration signals in a damaged UAV blade are exceedingly difficult to categorize, particularly in well-known intelligent drones where manufacturers provide continual stabilization even in the presence of faults, the suggested model provided a classification accuracy of more than 91%, demonstrating its reliability in predicting all tested situations.

For future work, each smart drone has an embedded accelerometer that generates flight data. With the DJI drones, acquiring flight data is simple by utilizing phone apps where pitching and rolling records in degrees are collected. These data may be transformed using numerical analysis into angular acceleration signals, resulting in vibration-based signals. This well-known method is limited to a relatively small data set of flight vibration signals and cannot be relied on to anticipate defects during preflight checks. The utilized accelerometer may be incorporated with a microcontroller to wirelessly record massive data of time–frequency domain vibration signals for enhanced imbalance prediction and accurate preflight testing.

Author Contributions: Methodology, A.A.J.; formal analysis, L.A.A.-H.; investigation, A.A.J.; writing—original draft, A.A.J.; writing—review and editing, A.A.J.; supervision, A.A.J. All authors have read and agreed to the published version of the manuscript.

Funding: This research received no external funding.

Data Availability Statement: Data are available upon reasonable request; please Email luttfi.a.alhaddad@uotechnology.edu.iq if you need the data.

Acknowledgments: The authors acknowledge the help of previous authors cited in this research article.

Conflicts of Interest: The authors declare no conflict of interest.

References

1. Zieja, M.; Golda, P.; Zokowski, M.; Majewski, P. Vibroacoustic technique for the fault diagnosis in a gear transmission of a military helicopter. *J. Vibroengineering* **2017**, *19*, 1039–1049. [CrossRef]
2. Sun, C.; Wang, Y.; Sun, G. A multi-criteria fusion feature selection algorithm for fault diagnosis of helicopter planetary gear train. *Chin. J. Aeronaut.* **2020**, *33*, 1549–1561. [CrossRef]
3. Krichen, M.; Adoni, W.Y.H.; Mihoub, A.; Alzahrani, M.Y.; Nahhal, T. Security Challenges for Drone Communications: Possible Threats, Attacks and Countermeasures. In Proceedings of the 2022 2nd International Conference of Smart Systems and Emerging Technologies (SMARTTECH), Riyadh, Saudi Arabia, 9–11 May 2022; pp. 184–189. [CrossRef]
4. Bunse, C.; Plotz, S. Security Analysis of Drone Communication Protocols. In *Engineering Secure Software and Systems. ESSoS 2018*; Lecture Notes in Computer Science; Payer, M., Rashid, A., Such, J., Eds.; Springer: Cham, Switzerland, 2018; Volume 10953. [CrossRef]
5. Karbach, N.; Bobrowski, N.; Hoffmann, T. Observing volcanoes with drones: Studies of volcanic plume chemistry with ultralight sensor systems. *Sci. Rep.* **2022**, *12*, 17890. [CrossRef]
6. Booysen, R.; Jackisch, R.; Lorenz, S.; Zimmermann, R.; Kirsch, M.; Nex, P.A.M.; Gloaguen, R. Detection of REEs with lightweight UAV-based hyperspectral imaging. *Sci. Rep.* **2020**, *10*, 17450. [CrossRef]
7. Munawar, H.S.; Ullah, F.; Heravi, A.; Thaheem, M.J.; Maqsoom, A. Inspecting Buildings Using Drones and Computer Vision: A Machine Learning Approach to Detect Cracks and Damages. *Drones* **2021**, *6*, 5. [CrossRef]
8. Brewer, M.J.; Clements, C.B. Meteorological Profiling in the Fire Environment Using UAS. *Fire* **2020**, *3*, 36. [CrossRef]
9. Puchalski, R.; Giernacki, W. UAV Fault Detection Methods, State-of-the-Art. *Drones* **2022**, *6*, 330. [CrossRef]
10. Medeiros, R.L.V.; Ramos, J.G.G.S.; Nascimento, T.P.; Filho, A.C.L.; Brito, A.V. A Novel Approach for Brushless DC Motors Characterization in Drones Based on Chaos. *Drones* **2018**, *2*, 14. [CrossRef]
11. Yang, P.; Geng, H.; Wen, C.; Liu, P. An Intelligent Quadrotor Fault Diagnosis Method Based on Novel Deep Residual Shrinkage Network. *Drones* **2021**, *5*, 133. [CrossRef]
12. Masalimov, K.; Muslimov, T.; Munasypov, R. Real-Time Monitoring of Parameters and Diagnostics of the Technical Condition of Small Unmanned Aerial Vehicle's (UAV) Units Based on Deep BiGRU-CNN Models. *Drones* **2022**, *6*, 368. [CrossRef]

13. Dai, W.; Liang, K.; Wang, B. State Monitoring Method for Tool Wear in Aerospace Manufacturing Processes Based on a Convolutional Neural Network (CNN). *Aerospace* **2021**, *8*, 335. [CrossRef]
14. Xu, Z.; Chen, B.; Zhou, S.; Chang, W.; Ji, X.; Wei, C.; Hou, W. A Text-Driven Aircraft Fault Diagnosis Model Based on a Word2vec and Priori-Knowledge Convolutional Neural Network. *Aerospace* **2021**, *8*, 112. [CrossRef]
15. Ai, S.; Song, J.; Cai, G.; Zhao, K. Active Fault-Tolerant Control for Quadrotor UAV against Sensor Fault Diagnosed by the Auto Sequential Random Forest. *Aerospace* **2022**, *9*, 518. [CrossRef]
16. Wild, G.; Gavin, K.; Murray, J.; Silva, J.; Baxter, G. A Post-Accident Analysis of Civil Remotely-Piloted Aircraft System Accidents and Incidents. *J. Aerosp. Technol. Manag.* **2017**, *9*, 157–168. [CrossRef]
17. Bhandari, S.; Jotautienė, E. Vibration Analysis of a Roller Bearing Condition Used in a Tangential Threshing Drum of a Combine Harvester for the Smooth and Continuous Performance of Agricultural Crop Harvesting. *Agriculture* **2022**, *12*, 1969. [CrossRef]
18. Yao, Y.; Li, X.; Yang, Z.; Li, L.; Geng, D.; Huang, P.; Li, Y.; Song, Z. Vibration Characteristics of Corn Combine Harvester with the Time-Varying Mass System under Non-Stationary Random Vibration. *Agriculture* **2022**, *12*, 1963. [CrossRef]
19. Oyarzun, J.; Aizpuru, I.; Baraia-Etxaburu, I. Time–Frequency Analysis of Experimental Measurements for the Determination of EMI Noise Generators in Power Converters. *Electronics* **2022**, *11*, 3898. [CrossRef]
20. Sadeghi, S.M.; Mashadi, B.; Amirkhani, A.; Salari, A.H. Maximum tire/road friction coefficient prediction based on vehicle vertical accelerations using wavelet transform and neural network. *J. Braz. Soc. Mech. Sci. Eng.* **2022**, *44*, 324. [CrossRef]
21. Leavey, C.M.; James, M.N.; Summerscales, J.; Sutton, R. An introduction to wavelet transforms: A tutorial approach. *Insight-Non-Destr. Test. Cond. Monit.* **2003**, *45*, 344–353. [CrossRef]
22. Rajbhandari, S. Application of Wavelets and Artificial Neural Network for Indoor Optical Wireless Communication Systems. Ph.D. Thesis, School of Computing, Engineering and Information Sciences, University of Northumbria, Newcastle, UK, 2009.
23. Giaouris, D.; Zahawi, B.; El-Murr, G.; Pickert, V. Application of Wavelet Transformation for the Identification of High Frequency Spurious Signals in Step Down DC—DC Converter Circuits Experiencing Intermittent Chaotic Patterns. In Proceedings of the 3rd IET International Conference on Power Electronics, Machines and Drives, Dublin, Ireland, 4–6 April 2006; pp. 394–397.
24. Loutas, T.; Kostopoulos, V. Utilising the wavelet transform in condition-based maintenance: A review with applications. In *Advances in Wavelet Theory and Their Applications in Engineering, Physics and Technology*; Baleanu, D., Ed.; InTech: Rijeka, Croatia, 2012; pp. 273–312. ISBN 978-953-51-0494-0.
25. Qu, J.; Zhang, Z.; Gong, T. A novel intelligent method for mechanical fault diagnosis based on dual-tree complex wave-let packet transform and multiple classifier fusion. *Neurocomputing* **2016**, *171*, 837–853. [CrossRef]
26. Ong, P.; Tieh, T.H.C.; Lai, K.H.; Lee, W.K.; Ismon, M. Efficient gear fault feature selection based on moth-flame optimisation in discrete wavelet packet analysis domain. *J. Braz. Soc. Mech. Sci. Eng.* **2019**, *41*, 266. [CrossRef]
27. Vivas, E.L.A.; Garcia-Gonzalez, A.; Figueroa, I.; Fuentes, R.Q. Discrete Wavelet Transform and ANFIS Classifier for Brain-Machine Interface based on EEG. In Proceedings of the 6th International Conference on Human System Interactions, Sopot, Poland, 6–8 June 2013; Paja, W.A., Wilamowski, B.M., Eds.; IEEE: New York, NY, USA, 2013; pp. 137–144.
28. Misiti, M.; Misiti, Y.; Oppenheim, G.; Poggi, J.-M. Wavelet Toolbox For Use with MATLAB: MathWorks. 1997. Available online: http://cda.psych.uiuc.edu/matlab_pdf/wavelet_ug.pdf (accessed on 2 October 2022).
29. Hariharan, M.; Fook, C.; Sindhu, R.; Ilias, B.; Yaacob, S. A comparative study of wavelet families for classification of wrist motions. *Comput. Electr. Eng.* **2012**, *38*, 1798–1807. [CrossRef]
30. Gonçalves, M.A.; Gonçalves, A.S.; Franca, T.C.C.; Santana, M.S.; da Cunha, E.F.F.; Ramalho, T.C. Improved Protocol for the Selection of Structures from Molecular Dynamics of Organic Systems in Solution: The Value of Investigating Different Wavelet Families. *J. Chem. Theory Comput.* **2022**, *18*, 5810–5818. [CrossRef] [PubMed]
31. Too, J.; Abdullah, A.R.; Saad, N.M.; Ali, N.M.; Musa, H. A Detail Study of Wavelet Families for EMG Pattern Recognition. *Int. J. Electr. Comput. Eng. (IJECE)* **2018**, *8*, 4221–4229. [CrossRef]
32. Jaber, A.A.; Bicker, R. The optimum selection of wavelet transform parameters for the purpose of fault detection in an industrial robot. In Proceedings of the 2014 IEEE International Conference on Control System, Computing and Engineering (ICCSCE 2014), Penang, Malaysia, 28–30 November 2014; pp. 304–309.
33. Katsavrias, C.; Papadimitriou, C.; Hillaris, A.; Balasis, G. Application of Wavelet Methods in the Investigation of Geospace Disturbances: A Review and an Evaluation of the Approach for Quantifying Wavelet Power. *Atmosphere* **2022**, *13*, 499. [CrossRef]
34. Ma, L.; Zhang, S.; Cheng, L. A 2D Daubechies wavelet model on the vibration of rectangular plates containing strip indentations with a parabolic thickness profile. *J. Sound Vib.* **2018**, *429*, 130–146. [CrossRef]
35. Su, B.; Xu, C.; Li, J. A Deep Neural Network Approach to Solving for Seal's Type Partial Integro-Differential Equation. *Mathematics* **2022**, *10*, 1504. [CrossRef]
36. Stanković, M.; Mirza, M.M.; Karabiyik, U. UAV Forensics: DJI Mini 2 Case Study. *Drones* **2021**, *5*, 49. [CrossRef]
37. Casabianca, P.; Zhang, Y. Acoustic-Based UAV Detection Using Late Fusion of Deep Neural Networks. *Drones* **2021**, *5*, 54. [CrossRef]
38. Ghazali, M.H.M.; Rahiman, W. An Investigation of the Reliability of Different Types of Sensors in the Real-Time Vibration-Based Anomaly Inspection in Drone. *Sensors* **2022**, *22*, 6015. [CrossRef]
39. Jaber, A.A.; Bicker, R. A simulation of non-stationary signal analysis using wavelet transform based on LabVIEW and Matlab. In Proceedings of the UKSim-AMSS 8th European Modelling Symposium on Computer Modelling and Simulation, EMS 2014, Pisa, Italy, 21–23 October 2014; pp. 138–144. [CrossRef]

40. Ewert, P.; Kowalski, C.T.; Orlowska-Kowalska, T. Low-Cost Monitoring and Diagnosis System for Rolling Bearing Faults of the Induction Motor Based on Neural Network Approach. *Electronics* **2020**, *9*, 1334. [CrossRef]
41. Jawad, S.M.; Jaber, A.A. Bearings Health Monitoring Based on Frequency-Domain Vibration Signals Analysis. *Eng. Technol. J.* **2022**, *41*, 86–95. [CrossRef]
42. Flaieh, E.H.; Hamdoon, F.O.; Jaber, A.A. Estimation the natural frequencies of a cracked shaft based on finite element modeling and artificial neural network. *Int. J. Adv. Sci. Eng. Inf. Technol.* **2020**, *10*, 1410–1416.
43. Jaber, A.A.; Bicker, R. Industrial robot fault detection based on statistical control chart. *Am. J. Eng. Appl. Sci.* **2016**, *9*, 251–263. [CrossRef]
44. Jaber, A.A.; Bicker, R. Development of a Condition Monitoring Algorithm for Industrial Robots based on Artificial Intelligence and Signal Processing Techniques. *Int. J. Electr. Comput. Eng. (IJECE)* **2018**, *8*, 996–1009. [CrossRef]
45. Dhomad, T.A.; Jaber, A. Bearing fault diagnosis using motor current signature analysis and the artificial neural network. *Int. J. Adv. Scince Eng. Inf. Technol.* **2020**, *10*, 70–79. [CrossRef]
46. Mohammed, J.S.; Abdulhady, J.A. Rolling bearing fault detection based on vibration signal analysis and cumulative sum control chart. *FME Trans.* **2021**, *49*, 684–695. [CrossRef]
47. Altinors, A.; Yol, F.; Yaman, O. A sound based method for fault detection with statistical feature extraction in UAV motors. *Appl. Acoust.* **2021**, *183*, 108325. [CrossRef]
48. Ma, L.; Fu, T.; Blaschke, T.; Li, M.; Tiede, D.; Zhou, Z.; Ma, X.; Chen, D. Evaluation of Feature Selection Methods for Object-Based Land Cover Mapping of Unmanned Aerial Vehicle Imagery Using Random Forest and Support Vector Machine Classifiers. *ISPRS Int. J. Geo-Inf.* **2017**, *6*, 51. [CrossRef]
49. Sarra, R.R.; Dinar, A.M.; Mohammed, M.A.; Abdulkareem, K.H. Enhanced Heart Disease Prediction Based on Machine Learning and χ^2 Statistical Optimal Feature Selection Model. *Designs* **2022**, *6*, 87. [CrossRef]
50. Demsar, J.; Zupan, B. Orange: Data mining fruitful and fun-A historical perspective. *Informatica* **2013**, *37*, 55–60.
51. Glowacz, A. Thermographic Fault Diagnosis of Shaft of BLDC Motor. *Sensors* **2022**, *22*, 8537. [CrossRef] [PubMed]
52. Al-Haddad, S.A.; Al-Ani, F.H.; Fattah, M.Y. Effect of Using Plastic Waste Bottles on Soil Response above Buried Pipes under Static Loads. *Appl. Sci.* **2022**, *12*, 12304. [CrossRef]